

Plasticity of Metal Nanowires

Christopher R. Weinberger*

Sandia National Laboratories, Albuquerque, New Mexico 87185-1411, USA

Wei Cai†

*Department of Mechanical Engineering,
Stanford University, CA 94305-4040*

(Dated: November 24, 2011)

Abstract

The mechanisms of plasticity in metal nanowires with diameters below 100 nm are reviewed. At these length scales, plasticity in face-centered-cubic metals subjected to uniaxial loading is dominated by dislocation nucleation from free surfaces, which has been studied extensively by molecular dynamics. These simulations show that nanowires can deform in a variety of ways including slip via perfect dislocations, partial dislocations and deformation twins. The competition between these mechanisms can be explained primarily through the Schmid factor and material properties, although surface orientation and roughness also contribute. The strength of these materials is very high and can be described by classical nucleation theory which predicts strong temperature and geometry dependence as well as a weak strain rate dependence. Additionally, nanowires exhibit, through twinning or phase transformation, pseudo-elastic and shape-memory behaviors which are attributed to their small size and the surface stress. The plasticity of nanowires subject to torsion and bending as well as those composed of body-centered-cubic metals are also summarized.

*Electronic address: crweinb@sandia.gov

†Electronic address: caiwei@stanford.edu

Contents

I. Introduction	3
II. Key concepts	5
A. Surface stress	6
B. Generalized Stacking Faults	8
C. Schmid Factor	11
III. Competition between slip and twinning	11
A. Effect of Schmid factor	13
B. Effect of generalized stacking fault energy	15
C. Effect of side surfaces	17
IV. Yield strength	19
A. Effect of Schmid factor and surface stress	21
B. Classical nucleation theory	22
C. Alternative nucleation criteria	24
V. Phase transformation	26
VI. Pseudo-elastic and shape memory effects	28
VII. Bending and Torsion	30
A. Bending	31
B. Torsion	31
C. Pseudo-elasticity of $\langle 110 \rangle$ NWs	33
VIII. BCC metal nanowires	33
IX. Summary and Outlook	35
Acknowledgments	37
References	37

I. INTRODUCTION

Nanowires have been a major focus for research at the nanoscale due to their unique properties and their potential as a fundamental building block of nanotechnology [1]. Complementing semiconductor nanowires, metal nanowires offer different mechanical [2], electrical [3, 4], magnetic [5], optical [6] and catalytic [7] properties, and are envisioned to be key components of nano-electro-mechanical-systems (NEMS) [8]. For example, rhodium (Rh) nanowires as nano-resonator arrays can be used for sensitive chip-based oligonucleotide detection [9]. Gold (Au) nanowires can grow inside individual nanotubes of Li⁺-intercalation material TiS₂ to provide electrical conductivity [10]. Metal nanowires swimming in solution in response to rotating electric or magnetic fields [11–13] can deliver molecular signals to specified cells with subcellular resolution. Striped nanorods with Au and platinum (Pt) sections can swim in aqueous solution by catalyzing the formation of oxygen bubbles at the Pt end [7]. In addition, the emerging ability to manipulate and observe individual nanowires during deformation presents an exciting opportunity to understand the plastic deformation mechanisms of metals at the nanoscale.

Nanowire fabrication is a diverse and continuously evolving field that deserves its own dedicated review paper [10]. Nonetheless, a review paper on nanowire plasticity would not be complete without some mention of the fabrication methods. Probably the most widely used fabrication technique is electrochemical deposition over a nanoporous template [5, 10, 14, 15] whereby the nanowire diameter is controlled by the pore size. Common templates include: porous alumina membranes via anodization of aluminum metal [10, 14] and track-etched polymeric membranes [5, 10]. The diameter of the nanowires fabricated by this approach ranges from 10's to 100's of nanometers. These nanowires usually consist of multiple crystalline grains with grain size equal the wire diameter. Recently, electrochemical deposition into PMMA resist patterned by electron beam lithography has been used to make Au and copper (Cu) nanopillars of diameters 25 to 750 nm [15]. Single crystal, nano-twinned, bi- and poly-crystal nanowires can be fabricated by this approach by controlling the deposition current density. Nanowires can also be obtained without using a template. In 1956, Brenner [16] fabricated micron and sub-micron whiskers via metal halide reduction, although this method has not yet been used to produce nanowires. A variety of metal nanowires with diameters as small as 20 nm have been recently grown using physical vapor deposition

over partially carbon-coated silicon substrates [17]. These nanowires are single crystalline with atomically smooth, faceted surfaces and contain no dislocations. Zheng [18] et al. created Au nanowires via cold welding two Au nano-particles together followed by mechanical stretching. The nanowires thus obtained usually contains a high density of twin boundaries. Besides the bottom-up synthesis approaches mentioned above, metal nanowires can also be fabricated using a top-down approach, e.g. by cutting them from free-standing metal thin films [19]. All of the methods mentioned above generally create metal nanowires aligned along one of the three principle axes: $\langle 111 \rangle$, $\langle 110 \rangle$ and $\langle 100 \rangle$. Additional fabrication methods will continue to emerge and contribute to the quality and the diversity of geometries of the nanowires fabricated.

The main purpose of this review is to summarize the current predictions on the inelastic deformation behaviors of metallic nanowires and compare them with available experiments. Since there are several review papers on plasticity in micro-pillars and sub-micrometer pillars [20, 21], this review will focus on true nanowires, those with diameters less than 100 nm where it is believed that dislocation nucleation becomes a controlling mechanism of plastic deformation. Since experiments are just beginning to emerge at this length scale, most of the review will focus on predictions from atomistic simulations with an attempt to rationalize those observations using continuum theories. Due to space constraints, this review is limited to initially perfect NWs. Simulations [22–26] and experiments [27–29] on NWs containing internal twin boundaries or grain boundaries are not discussed.

The main types of inelastic deformation one expects to see in metallic nanowires are slip through perfect and partial dislocations, deformation twinning, and phase transformation. When the dominant deformation mechanism is deformation twinning or phase transformation, it can give rise to pseudo-elasticity and shape memory effects. This review will focus on the effects of shape, orientation, size and material on the inelastic deformation mechanisms.

There are several key concepts that are essential to the discussion of nanowire plasticity. The first is the realization that face-centered-cubic (FCC) nanowires of diameters $d \lesssim 100$ nm are expected to be dislocation starved [30]. This means that, in general, at the onset of yielding, there are no mobile dislocations inside the nanowire to contribute to plastic deformation. Therefore, plastic deformation is controlled by dislocation nucleation. In other crystal systems, such as body-centered-cubic (BCC) metals, the idea of dislocation starvation has not been well established and it is uncertain if mobile dislocations will be present in

these small volumes. Nonetheless, at least in FCC nanowires, the competition between mechanisms, such as perfect dislocation slip, partial dislocation slip and twinning, should be explained by their differences in nucleation energy barriers. The effects of orientation on the choice of deformation mechanisms in uniaxial loading can be largely accounted for by the Schmid factor which describes the resolved shear stress on a given slip system. The intrinsic material parameters that affect dislocation nucleation are the unstable stacking fault energy, the intrinsic stacking fault energy and the unstable twinning energy.

Another set of important concepts include surface energy and surface stress. Due to the small sizes of nanowires, the surface stress induces a high compressive stress in the nanowire interior. This leads to the size-dependent yield strength as well as the pseudo-elastic and shape memory effects in nanowires. Finally, from the simulation perspective one must be mindful of artifacts that arise from time-scale limitations and inaccuracies of the interatomic potentials used.

This review is organized into the following sections. Section II reviews the key concepts that are essential for understanding nanowire plasticity. This background is provided for those readers unfamiliar with the field of small scale mechanical properties. Section III reviews the competition between slip via partial dislocations, perfect dislocations and deformation twinning. Section IV discusses the size and orientation effects on the yield strength of metal nanowires. Section V covers the phenomenon of phase transformations in FCC and intermetallic nanowires. Section VI discusses pseudo-elastic and shape memory effects. Section VII discusses the behavior of FCC nanowires under bending and torsion. Section VIII discusses BCC metal nanowires under uniaxial loading. Section IX gives a short summary and discusses future directions for research.

II. KEY CONCEPTS

There are several key concepts that will be used throughout this review to understand the mechanics and plasticity in metallic nanowires (NWs). It will be useful to address these concepts here prior to discussing the literature.

A. Surface stress

Since NWs, like all nano-structures, have a high surface to volume ratio, the energy of the free surfaces and resulting surface stress becomes important. The surface energy depends on the surface orientation. Unfortunately, it has been extremely difficult to measure the surface energy anisotropy of metals by experiments [31]. The surface energy of a wide range of FCC and BCC metals have been predicted by first-principles calculations based on the density functional theory (DFT). The full-potential (FP) model [32] is presumably more accurate than the full charge density (FCD) model [33]. These calculations predict that for FCC metals the lowest energy facet is the {111}, followed by {100} and then the {110} [32]. The predicted surface energies of these facets for the four FCC metals (Al, Au, Cu, Ni) to be discussed in this review are in the range of 1 to 2.5 J·m⁻², consistent with experimental measurements [31, 34]. For BCC metals, the {110} and the {100} facets usually have lower energy than the {111} [33]. The predicted surface energies of these facets for BCC Mo, Ta, Fe are in the range of 2.2 to 3.9 J·m⁻², also consistent with experimental measurements [31, 34]. The anisotropy of the surface energy is believed to lead to strong faceting. For example, Richter et al. [17] have shown that in their as grown FCC metal NWs, most are oriented along the ⟨110⟩ direction and have {111} and {100} surface facets in agreement with the Wulff construction [35].

The atoms at metal surfaces are usually under-coordinated (i.e. having fewer neighbors than atoms in the bulk) and therefore tend to contract towards each other creating a tensile surface stress. For liquids, this is often termed the surface tension, which equals to the surface energy γ , because the atoms on the surface are free to move to the interior of the liquid [36]. In a crystalline solid, however, the limited atomic mobility makes the surface stress, f_{ij} , generally different from the surface energy γ . The surface stress f_{ij} can be written in terms of the surface strain e_{ij} as:

$$f_{ij} \equiv \frac{1}{A} \frac{\partial(A\gamma)}{\partial e_{ij}} = \gamma \delta_{ij} + \frac{\partial \gamma}{\partial e_{ij}}. \quad (1)$$

where A is the surface area. The surface strain and surface stress are both second rank tensors such that the free indices i and j run from 1 to 2, representing the two directions in the plane of the exposed free surfaces [36, 37]. The surface stress has units of J·m⁻², in contrast to the ordinary stress, which has units of J·m⁻³.

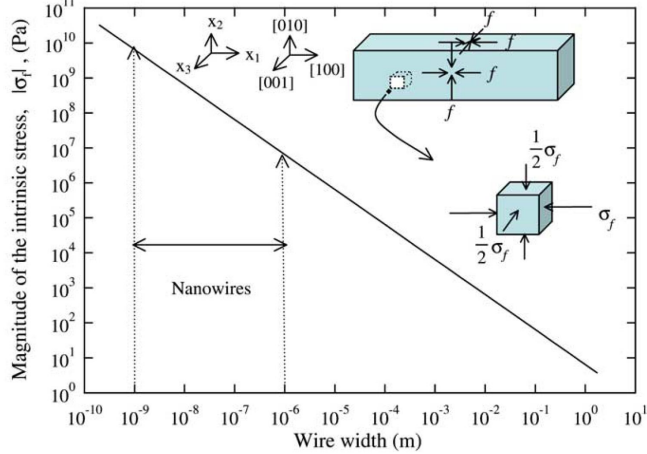


FIG. 1: The variation of the induced compressive stress in NW with the width of the NW.
(Reprinted with permission from [40].)

The presence of a tensile surface stress induces a compressive stress in the NW interior that scales inversely with the NW width. A simple scenario given by Diao et al. [38] illustrates the effects of surface stress on NWs. Consider a NW with a square cross section and width d , as shown in Fig. 1. Hence its cross sectional area is $A = d^2$. Let the magnitude of the surface stress be f , which is usually of the same order of magnitude as the surface energies. The average induced compressive stress along the NW axis on the NW interior can be written as:

$$\sigma_f = -\frac{4fd}{A} = -\frac{4f}{d} \quad (2)$$

Thus, the induced compressive stresses in the NW interior scale inversely with the wire width d . Assuming a nominal value of $f = 1 \text{ J} \cdot \text{m}^{-2}$, the induced compressive stress is shown in Fig. 1. For NW diameter in the range of 1 nm to 100 nm, the stresses range from 100's of MPa to several GPa. On the other hand, wires with diameters in the millimeter range would have interior stresses on the order of 1 MPa. This example oversimplifies the physics by ignoring the effects of the sharp corners [39], which give rise to stress concentrations. Nonetheless, Eq. (2) gives the correct scaling behavior of the induced stress on the NW interior and shows that this stress can significantly impact the mechanical properties of metallic NWs since it can approach the ideal strength of the metal.

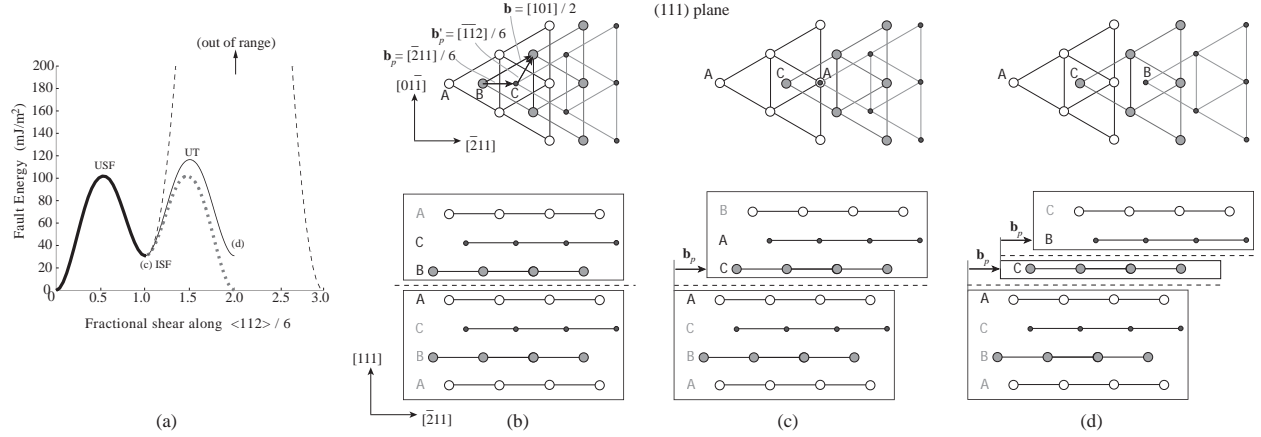


FIG. 2: (a) GSF curves of FCC Au predicted by the EAM Foiles potential [44]. The thick solid line corresponds to slip along $\mathbf{b}_p = \frac{1}{6}[\bar{2}11]$ from (b) the perfect FCC crystal structure to (c) the intrinsic stacking fault (ISF) structure. The dashed line corresponds to continued slip along the same \mathbf{b}_p direction. The dotted line corresponds to slip on the same (111) plane starting from the (c) ISF structure but along $\mathbf{b}'_p = \frac{1}{6}[\bar{1}\bar{1}2]$. The thin solid line corresponds to slip from the (c) ISF structure on the adjacent (111) plane to the twin structure in (d). \mathbf{b}_p and \mathbf{b}'_p are two partial dislocation Burgers vectors, which add up to the perfect Burgers vector $\mathbf{b} = \frac{1}{2}[\bar{1}01]$. The unstable stacking fault (USF) and unstable twinning (UT) energies are local maxima on the GSF curves (see text).

B. Generalized Stacking Faults

The second set of key concepts are the generalized stacking fault (GSF) energy and twinning energy curves. The GSF energy curve was introduced by Vitek [41] as a method to predict dislocation core structures, and Rice [42] initially used the GSF energy curve in models of dislocation nucleation. The GSF energy curve is defined in a specific slip direction on a specific slip plane in a crystal. For FCC metals, slip occurs on {111} planes and along the $\langle 110 \rangle$ directions. However, an elementary slip step along the $\langle 110 \rangle$ direction is usually composed of two sub-steps along the $\langle 112 \rangle$ directions. In dislocation theory [43], this corresponds to the dissociation of perfect dislocations with Burgers vector $\frac{1}{2}\langle 110 \rangle$ into partial dislocations with Burgers vector $\frac{1}{6}\langle 112 \rangle$. Hence in FCC metals the GSF curves are typically computed on {111} plane and along the $\langle 112 \rangle$ direction.

Fig. 2(a) shows the GSF curves for FCC Au predicted by an embedded-atom method

(EAM) potential. To understand the meaning of the GSF curves, let us start with the perfect FCC crystal structure shown in Fig. 2(b). The FCC structure can be considered as three types of (111) atomic layers stacked on top each other in the sequence of $\cdots \text{ABCABC}\cdots$, each layer forming a triangular lattice. Now consider a (111) plane (dashed line) cutting the crystal into two halves between layer A and layer B, and displacing the upper half of the crystal relative to the lower half along the direction of $\mathbf{b}_p = \frac{1}{6}[\bar{2}11]$. During this displacement, both halves of the crystal remain as rigid blocks. The energy in excess of the perfect crystal per unit area of the cut plane as a function of the displacement is a GSF curve. If the relative distance between the two blocks along the [111] direction is allowed to relax, the result is called the relaxed GSF energy; otherwise the result is called the unrelaxed GSF energy. The thick solid line in Fig. 2(a) shows an unrelaxed GSF energy curve. When the relative displacement along the $[\bar{2}11]$ direction exactly equals $|\mathbf{b}_p|$, an intrinsic stacking fault (ISF) is created, as shown in Fig. 2(c). The layer above the cut plane now assume the position of layer C. The excess energy per unit area is γ_{ISF} , which is $31 \text{ mJ} \cdot \text{m}^{-2}$ in this plot. The maximum on the GSF curve between the origin and ISF is the unstable stacking fault (USF) energy, γ_{USF} , $102 \text{ mJ} \cdot \text{m}^{-2}$ here, which is a measure of the barrier for the nucleation of a leading partial dislocation in a perfect crystal. The maximum slope of the GSF curve between the origin and USF has the unit of stress, and is often interpreted as the ideal shear strength of the crystal.

If the displacement continues along the same $[\bar{2}11]$ direction passing the ISF point, the corresponding GSF energy rises to very high values, shown as the dashed line in Fig. 2(a). In a real crystal, sliding between atomic layers rarely follows this portion of the GSF curve. Instead, once the ISF point is reached, sliding will continue along a different $\langle 112 \rangle$ direction, e.g. $\mathbf{b}'_p = \frac{1}{6}[\bar{1}12]$, and the GSF curve takes the shape of the dotted line in Fig. 2(a). In dislocation theory, \mathbf{b}_p and \mathbf{b}'_p are the Burgers vectors of the leading and trailing partial dislocations forming a perfect dislocation.

Sliding between (111) atomic layers can continue in a different manner after an ISF is formed. Sliding can initiate along the same \mathbf{b}_p direction on the (111) plane immediately above the ISF. Fig. 2(d) shows the structure when the sliding on the second (111) plane also equals $|\mathbf{b}_p|$. Notice that the three atomic layers adjacent to the two (111) slip planes now has the stacking sequence of ACB, which is exactly the mirror image of the original FCC stacking, ABC. Therefore, the structure in Fig. 2(d) contains a thin plate of twinned

TABLE I: Important features on the (unrelaxed) GSF curves for various FCC metals as computed using EAM [46] and tight binding (TB) model [47]. The twinnability parameter τ_a [48] as well as other ratios are listed to compare different metals.

	EAM [46]				TB [47]		
	Cu	Ni	Au	Al	Cu	Au	Al
γ_{ISF} (mJ·m ⁻²)	45	125	31	146	64	49	99
γ_{USF} (mJ·m ⁻²)	180	402	101	189	200	110	164
γ_{UT} (mJ·m ⁻²)	202	460	122	240	236	135	207
$\tau_a \equiv \left(1.136 - 0.151 \frac{\gamma_{\text{ISF}}}{\gamma_{\text{USF}}} \right) \sqrt{\frac{\gamma_{\text{USF}}}{\gamma_{\text{UT}}}}$	1.037	1.018	0.991	0.905	1.001	0.965	0.930
$\gamma_{\text{USF}}/\gamma_{\text{UT}}$	0.891	0.874	0.828	0.788	0.848	0.815	0.792
$\gamma_{\text{USF}}/(\gamma_{\text{UT}} - \gamma_{\text{ISF}})$	1.147	1.200	1.110	2.011	1.163	1.280	1.519
$(\gamma_{\text{USF}} - \gamma_{\text{ISF}})/(\gamma_{\text{UT}} - \gamma_{\text{ISF}})$	0.860	0.827	0.769	0.457	0.791	0.709	0.602

FCC crystal, which can grow in thickness if slip continues on adjacent (111) planes one after another. The excess energy per unit area for the structure in Fig. 2(d) is twice the twin interface energy γ_T . The excess energy per unit area as a function of slip when going from Fig. 2(c) to (d) is plotted as a thin grey line in Fig. 2(a). The maximum along this line is the unstable twinning (UT) energy [45], γ_{UT} , which is 117 mJ · m⁻² here. The difference between γ_{UT} and γ_{ISF} is a measure of the energy barrier against the nucleation of twinning on top of an already formed intrinsic stacking fault.

The ISF, USF and UT energies are the most important features on GSF curves and strongly influence the plastic deformation mechanisms of FCC metal NWs. Table I list the values of these energies and their ratios for four FCC metals. The values predicted by the embedded-atom method (EAM) potential [46] are listed because this is the most widely used model in existing molecular dynamics simulations of NW plasticity. The values predicted by the tight-binding (TB) model [47] are also listed for comparison. We note that these generalized stacking fault energies are about one order of magnitude lower than the surface energy γ discussed in the previous subsection.

C. Schmid Factor

The Schmid factor will be used extensively in this review to explain the orientation dependence of NW plasticity. For bulk crystals, the Schmid law [49, 50] states that plasticity occurs on a slip system when the shear stress acting on the plane and along the slip direction reaches a critical value. Under uniaxial loading, the most active slip system, or the one with the highest resolved shear stress, can be determined from a purely geometric factor known as the Schmid factor. Consider a uniaxially loaded bar together with a given slip plane and slip direction, as shown in Fig. 3. The loading axis makes an angle χ with respect to the slip plane normal, and an angle ϕ with respect to the slip direction. Using simple geometry, the resolved shear stress on the slip system (i.e. slip plane plus slip direction), τ_{RSS} , can be related to the applied uniaxial stress σ through the relation $\tau_{RSS} = \sigma \cos(\chi) \cos(\phi)$. From this relation the Schmid factor [43] is defined as: $S \equiv \cos(\chi) \cos(\phi)$, which is a purely geometric factor in the range of $0 \leq S \leq 1/2$. Under the Schmid law, plastic flow occurs on a slip system when the resolved shear stress reaches a critical value: $\tau_{RSS} = \tau_{CRSS}$. As the applied load increases, slip is thus expected to first occur on the slip system with the highest Schmid factor. The Schmid law is also often interpreted to suggest that the most active slip system is the one with the highest Schmid factor. The Schmid law is well obeyed in bulk FCC and HCP (hexagonal close packed) metals, in which the critical resolved shear stress is the stress required to move existing dislocations away from pinning points. In FCC NWs, we also expect the Schmid factor to play an important role in initiating plastic deformation, but through the nucleation of new dislocations.

III. COMPETITION BETWEEN SLIP AND TWINNING

Slip and twinning are two major plastic deformation mechanisms for bulk metals [50]. It is therefore not surprising that both slip and twinning have been observed in molecular dynamics (MD) simulations of metal NWs. However, slip in NWs can be carried out either by perfect dislocations or by partial dislocations, see Fig. 4, which is a further complication brought about by the small dimensions of the NWs. In bulk metals, the competition between the various deformation mechanisms is influenced by temperature and the loading type (e.g. tension or compression). In metal NWs, this competition is additionally influenced by the

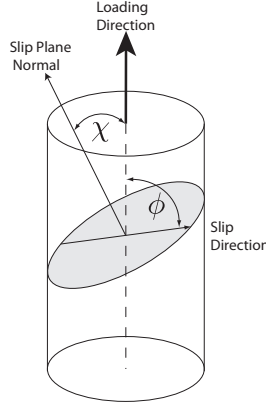


FIG. 3: A crystal that is loaded uniaxially illustrating the slip plane and slip direction.

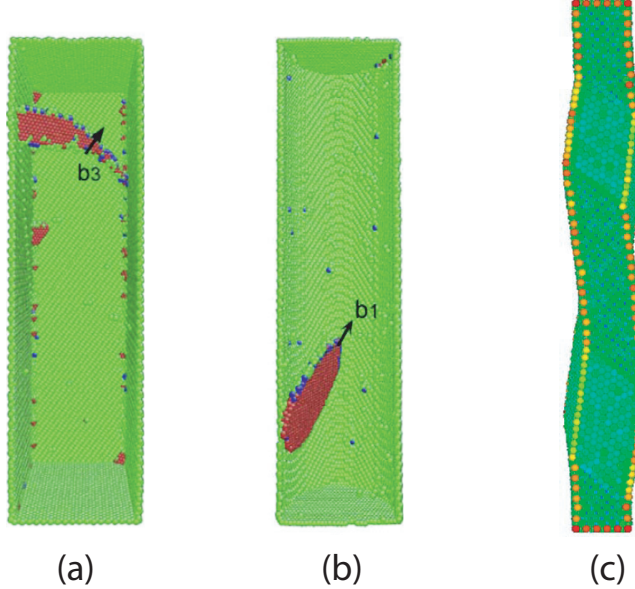


FIG. 4: (a) Slip by perfect dislocation (f-slip) in Cu $\langle 111 \rangle$ NW under compressive loading [53]. (b) Slip by partial dislocation (p-slip) in Cu $\langle 111 \rangle$ NW under tensile loading [53]. (c) Twinning in Cu $\langle 110 \rangle$ NW under tensile loading [51]. (Reprinted with permission from [53] and [51].)

orientation and diameter of the wires, as well as the orientation of their side surfaces [51] and other geometric factors [52]. Understanding how the deformation mechanism in NWs depends on these variables is essential for accurate predictions of the mechanical strength of NWs.

Table II summarizes the deformation mechanisms of FCC metal NWs right after yield

TABLE II: Summary of the deformation mechanisms of FCC metal NWs observed in MD simulations. Slip by perfect (full) dislocations, slip by partial dislocations and twinning are indicated by f-slip, p-slip and twin, respectively. Tension and compression loading types are indicated by T and C, respectively. The predicted mechanisms based on the Schmid factor and GSF are also listed.

orientation	loading type	side surface	observed mechanism	prediction from Schmid factor	from Schmid factor & GSF	metal
$\langle 100 \rangle$	T	{100}	f-slip & p-slip	f-slip	f-slip	Au [40, 44]
	T	{100}	p-slip / twin ^a	f-slip	f-slip	Cu [52, 54]
	C	{100}	twin	twin / p-slip	twin	Au, Cu, Ni [46, 51]
	C	{110}	p-slip	twin / p-slip	twin	Au, Cu, Ni [51]
	C	cylindrical	twin	twin / p-slip	twin	Au [55, 56]
$\langle 110 \rangle$	T	{110}, {001}	p-slip	twin / p-slip	twin	Au, Cu, Ni [51]
	T	{111}	twin	twin / p-slip	twin	Cu, Ni [46, 57]
	T	{111}	twin / p-slip ^b	twin / p-slip	twin	Au [46, 51, 57]
	T	{111}	f-slip	twin / p-slip	f-slip	Al [46]
	C	{110}, {001}	f-slip & p-slip	f-slip	f-slip	Au, Cu, Ni [51]
	C	{111}	N/A ^c	f-slip	f-slip	Au, Cu, Ni [51]
	C	cylindrical	f-slip	f-slip	f-slip	Au [55]
$\langle 111 \rangle$	T	{110}, {112}	p-slip	twin / p-slip	twin	Au [40], Cu [53]
	T	cylindrical	p-slip	twin / p-slip	twin	Cu [53]
	C	{110}, {112}	f-slip & p-slip	f-slip	f-slip	Au [40]
	C	{110}, {112}	f-slip	f-slip	f-slip	Cu [53]
	C	cylindrical	f-slip	f-slip	f-slip	Au, Cu [53, 55]

^aP-slip and twinning are reported for NWs with square and rectangular cross sections, respectively [52].

^bTwinning is observed at 5 K and 50 K but not at 200 K in [46] but is observed at 300 K in [51, 57].

^cNo dislocation or twinning is observed. Atoms pile up around the fixed edges of the NW [51].

as observed in MD simulations. The most extensively studied NWs are made of Au and Cu, followed by Ni and Al. Slip by perfect (full) dislocations, slip by partial dislocations, and twinning are indicated by f-slip, p-slip and twin, respectively. Which deformation mechanism occurs is influenced strongly by the NW orientation and loading type (tension or compression) [40, 51, 53]. This influence can be explained, to a large extent, by the Schmid factors of the partial dislocations on the {111} slip planes (with the notable exception of Cu ⟨100⟩ NWs with {100} side surfaces in tension). However, the Schmid factor alone cannot distinguish between p-slip and twinning. Which one of these two mechanisms is favored over the other depends on the material property (e.g. the “twinnability” parameter [48]), as well as the side surfaces of the NWs. These effects will be discussed in the following subsections.

To reduce computational cost, most of the existing MD simulations are limited to NWs with diameters less than 20 nm. It is believed that the trends in deformation mechanisms identified in these simulations are still valid for diameters up to 100 nm, for which the plastic deformation are still controlled by dislocation nucleation. While this belief is reasonable, it is of interest to confirm it by performing MD simulations up to 100 nm diameters.

A. Effect of Schmid factor

All the MD simulations listed in Table II started with NWs that are free from any lattice defects, such as dislocations or stacking faults. In most simulations, yield occurs with the nucleation of a dislocation from the NW surface. The type of dislocation nucleation event usually falls into the following two categories.

1. A perfect dislocation is nucleated from the surface. Alternatively, this can be described as the nucleation of a leading partial dislocation which is immediately followed by the trailing partial on the same slip plane. This leads to slip by perfect dislocations (f-slip).
2. A leading partial dislocation is nucleated from the surface, but is not followed by a trailing partial on the same slip plane. Instead, additional leading partial dislocations are nucleated on parallel slip planes (or other slip planes related by symmetry). If the next partial dislocation is nucleated on a parallel slip plane immediately above the plane of the first partial (see Fig. 2(d)), then twinning (twin) occurs. Otherwise, slip by partial dislocation (p-slip) occurs.

TABLE III: Schmid factors for partial and perfect dislocations in FCC metal NWs under different loading conditions. The loading types and predicted deformation mechanisms are specified in the same way as in Table II.

orientation	loading type	leading partial	trailing partial	perfect dislocation	predicted deformation mechanism
$\langle 100 \rangle$	T	0.24	0.47	0.41	f-slip
	C	0.47	0.24	0.41	twin / p-slip
$\langle 110 \rangle$	T	0.47	0.24	0.41	twin / p-slip
	C	0.24	0.47	0.41	f-slip
$\langle 111 \rangle$	T	0.31	0.16	0.27	f-slip
	C	0.16	0.31	0.27	twin / p-slip

Whether scenario 1 or 2 occurs can be predicted by considering the Schmid factors of the leading and trailing partial dislocations on the $\{111\}$ slip plane [51], as listed in Table III. If the Schmid factor of the trailing partial is larger than that of the leading partial, then either the perfect dislocation is expected to nucleate directly, or the nucleation of the trailing partial is expected to immediately follow the nucleation of the leading partial, resulting in scenario 1 (f-slip). This is the case for $\langle 100 \rangle$ and $\langle 111 \rangle$ NWs in tension and $\langle 110 \rangle$ NWs in compression. If, on the other hand, the Schmid factor of the leading partial is larger than that of the trailing partial, then the leading partial alone is expected to nucleate, resulting in scenario 2 (twin or p-slip). This is the case for $\langle 100 \rangle$ and $\langle 111 \rangle$ NWs in compression and $\langle 110 \rangle$ NWs in tension.

Table II shows that the prediction from Schmid factor considerations is largely consistent with MD observations. When f-slip is predicted, f-slip is almost always observed, sometimes accompanied by p-slip. The observation of some p-slip is not necessarily a contradiction to the predictions because it is possible that on certain slip planes the trailing partial may not have nucleated at the time of observation but may do so shortly afterward. A notable exception is the observation of p-slip and twinning in $\langle 100 \rangle$ Cu NWs with $\{100\}$ side surfaces [52], even though f-slip is predicted based on Schmid factor considerations. This break-down of the Schmid law may be attributed to the unique ability of the $\{100\}$ side surfaces to reori-

ent to the more stable $\{111\}$ surfaces (see Section III C). Another exception is the case of $\langle 110 \rangle$ NWs with $\{111\}$ side surfaces under compression, in which deformation proceeds by atoms piling up around the fixed end of the NWs, instead of through the predicted f-slip mechanism. This observation may also be attributed to the stability of $\{111\}$ side surfaces.

When f-slip is not favored from Schmid factor considerations, either twinning or p-slip is almost always observed. The only exception is $\langle 110 \rangle$ Al NW loaded in tension, where f-slip is observed even though it is not favored from Schmid factor considerations [46]. This discrepancy is caused by the high stacking fault energy of Al, and will be removed in the next subsection when the generalized stacking fault energies are considered.

It is remarkable that the Schmid factor considerations, being purely geometric in nature, can explain many of the features observed in these MD simulations. However, the Schmid factor alone does not distinguish twinning versus p-slip, both occurring through the nucleation of the leading partial. From Table II, it appears that p-slip is more favorable for the $\langle 111 \rangle$ NWs (in tension), while twinning is more favorable for the $\langle 100 \rangle$ NWs (in compression) and the $\langle 110 \rangle$ NWs (in tension). However, it is not clear whether a responsible physical mechanism can be identified.

B. Effect of generalized stacking fault energy

As noted before, the Schmid factor cannot distinguish between p-slip and twinning. Therefore, some other criterion is needed to distinguish between the two. MD simulations show that the competition between twinning and p-slip is material dependent. As shown in Table II, Cu and Ni NWs with $\langle 110 \rangle$ orientation and $\{111\}$ side surfaces deform by twinning in tension [46, 57]. However, Au NWs under identical conditions would twin at low temperatures and slip (by partial dislocations) at higher temperatures and Al NWs deform by slip via perfect dislocations (f-slip) [46]. To understand this material dependence, the twinnability parameter derived by Tadmor and Bernstein [48] has been used to rank the propensity of the materials to twin [46]. The twinnability parameter τ_a is defined through the intrinsic stacking fault energy γ_{ISF} , the unstable stacking fault energy γ_{USF} , and the unstable twinning energy γ_{UT} . Table I gives the definition of τ_a and lists its values for Cu, Au, Ni and Al. The twinnability of these FCC metals can be ranked as, $\tau_a^{\text{Cu}} > \tau_a^{\text{Ni}} > \tau_a^{\text{Au}} > \tau_a^{\text{Al}}$. This trend is consistent with the MD observations of $\langle 110 \rangle$ NWs with $\{111\}$ side surfaces

loaded in tension.

While the twinnability parameter provides a qualitative ranking of the FCC metals in terms of their tendency to twin, the context in which this parameter is derived does not exactly match the conditions of these NW simulations. First, twinnability was derived by considering nucleation from a crack tip, but no cracks exist in the NWs at the onset of plastic deformation. Second, τ_a is obtained by averaging over all orientations in a polycrystal, whereas the NWs here are single crystals under uniaxial loading with well defined Schmid factors. Third, twinnability is designed to distinguish between f-slip and twinning, and is unable to select from *three* candidate mechanisms: p-slip, f-slip and twinning.

In the following, we describe a two-parameter criterion based on both the Schmid factor and the generalized stacking fault energies. Consider the scenario that a leading partial has already nucleated from the surface of the NW. Three possible events can occur next. First, another leading partial can nucleate on a parallel plane *not* adjacent to the first slip plane. This leads to p-slip, and the critical (axial) stress can be estimated from the maximum slope of the GSF curve from origin to USF, i.e., $\sigma_p^c = \alpha \gamma_{\text{USF}} / (b_p S_{\text{lead}})$, where $\alpha \approx \pi$ is a geometric factor, b_p is the magnitude of the partial Burgers vector, and S_{lead} is the Schmid factor of the leading partial. Second, the trailing partial can nucleate on the same slip plane of the leading partial. This leads to f-slip, and the critical stress can be estimated from the maximum slope of the GSF curve between ISF and USF (dotted line in Fig. 2(a)), i.e., $\sigma_f^c = \alpha (\gamma_{\text{USF}} - \gamma_{\text{ISF}}) / (b_p S_{\text{trail}})$, where S_{trail} is the Schmid factor of the trailing partial. Third, a leading partial can nucleate on the slip plane adjacent to the first leading partial. This leads to twinning, and its critical stress can be estimated as, $\sigma_t^c = \alpha (\gamma_{\text{UT}} - \gamma_{\text{ISF}}) / (b_p S_{\text{lead}})$. In this model, the event with the lowest critical stress is predicted to occur. The situation can be visualized in a map spanned by two parameters,

$$\tau_1 \equiv \frac{\sigma_p^c}{\sigma_t^c} = \frac{\gamma_{\text{USF}}}{\gamma_{\text{UT}} - \gamma_{\text{ISF}}} \quad (3)$$

$$\tau_2 \equiv \frac{\sigma_f^c}{\sigma_t^c} = \frac{\gamma_{\text{USF}} - \gamma_{\text{ISF}}}{\gamma_{\text{UT}} - \gamma_{\text{ISF}}} \cdot \frac{S_{\text{lead}}}{S_{\text{trail}}} \quad (4)$$

As shown in Fig. 5, the parameter space can be divided into three domains, corresponding to p-slip, f-slip and twin, respectively, depending on the relative magnitude of τ_1 , τ_2 and 1. To a very good approximation, $S_{\text{lead}}/S_{\text{trail}}$ only takes two possible values for all six loading conditions listed in Table III, i.e. $S_{\text{lead}}/S_{\text{trail}} \approx 0.51$ for $\langle 100 \rangle$ T, $\langle 110 \rangle$ C, $\langle 111 \rangle$ C, and $S_{\text{lead}}/S_{\text{trail}} \approx 1.95$ for $\langle 100 \rangle$ C, $\langle 110 \rangle$ T, $\langle 111 \rangle$ T. Therefore, each point in Fig. 5 represents

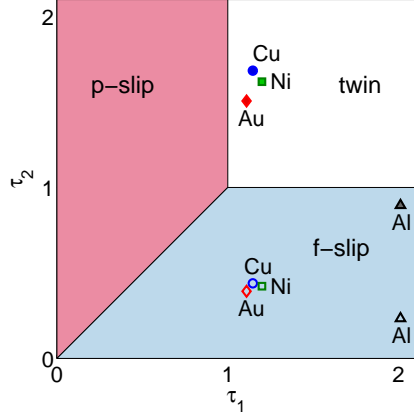


FIG. 5: Deformation mechanism map of FCC metal NWs under different axial loading conditions. The p-slip domain: $\tau_1 < \tau_2$ and $\tau_1 < 1$. The f-slip domain: $\tau_2 < \tau_1$ and $\tau_2 < 1$. The twin domain: $\tau_1 > 1$ and $\tau_2 > 1$. Open symbols correspond to the loading conditions of $\langle 100 \rangle$ tension, $\langle 110 \rangle$ compression, $\langle 111 \rangle$ compression. Filled symbols correspond to the loading condition of $\langle 100 \rangle$ compression, $\langle 110 \rangle$ tension, $\langle 111 \rangle$ tension.

one NW material and three loading conditions.

Fig. 5 shows that under $\langle 100 \rangle$ T, $\langle 110 \rangle$ C, and $\langle 111 \rangle$ C loading conditions, all four metals fall within the domain of f-slip, consistent with MD observations and the predictions based on Schmid factor alone. Under $\langle 100 \rangle$ C, $\langle 110 \rangle$ T, and $\langle 111 \rangle$ T loading conditions, Al falls within the domain of f-slip, consistent with MD observations [46], while Cu, Ni, Au all fall in the domain of twinning. These predictions are also listed in Table II.

The present model predicts that, as long as f-slip is not the dominant mechanism, twinning is always favored over p-slip. This is not entirely consistent with MD simulations, summarized in Table II, in which p-slip are observed under certain conditions. However, both p-slip and twinning occur through the stochastic event of dislocation nucleation, so that the boundary between the two mechanisms is not abrupt. In addition, if one accounts for the finite temperate and high strain rate in MD simulations, the boundary between p-slip and twin should shift to the right. This is because the nucleation rate of p-slip will be enhanced by the availability of multiple nucleation sites on the NW surface. We note that in Fig. 5, the points for Au, Cu and Ni lie close to the boundary between p-slip and twin. Au lies closest to the boundary, which is consistent with the greater tendency of Au toward p-slip as observed in MD simulations.

C. Effect of side surfaces

Table II shows that the competition between p-slip and twinning is influenced by the side surfaces of $\langle 100 \rangle$ and $\langle 110 \rangle$ oriented NWs. Neither the Schmid factor nor the generalized stacking fault energies, as discussed in the above two subsections, can account for the effect of side surfaces on deformation mechanisms. The effect of the side surface orientation can be accounted for, in principle, by considering surface step energies. The nucleation of an isolated partial dislocation from NWs with smooth surfaces will lead to a surface step, and the step energy increases the free energy barrier for p-slip nucleation. The nucleation of another partial dislocation on the slip plane immediately above that of the first partial (i.e. forming a micro-twin) may incur a lower step energy cost, if it effectively reorients the side surface to a lower energy facet. This explains why $\langle 100 \rangle$ NWs with $\{100\}$ side surface deform by twinning in compression (because they reorient to $\{111\}$ after twinning), while those with $\{110\}$ and $\{001\}$ surfaces deform by p-slip.

An aspect that has been ignored in the above discussions and MD simulations is that even high quality as-fabricated NWs have some surface roughness. Surface roughness produces local stress concentrations which promote dislocation nucleation around a small region. This favors twinning, which requires sequential nucleation of leading partials on adjacent slip planes. Therefore, even if p-slip is predicted by MD simulations, we would expect to find thin twin lamella in experiments, with the thickness of the lamellae determined by the roughness of the side surface. In the experiment by Zheng et al. [18], the dominant deformation mechanism in $\langle 100 \rangle$ Au nanocrystals loaded in tension is f-slip, consistent with Table II. However, limited twinning also occurs in the same loading condition, which is probably caused by the local surface roughness.

It is worth noting that some MD simulations predict that $\langle 110 \rangle$ Au NWs deform in tension by twinning at very low temperatures but transition to p-slip at temperatures above 200 K [46]. One explanation is that the relative influence of the step energy reduces with temperature as the size of the critical dislocation nucleus increases. The explicit temperature dependence of GSF energies [58] can also lead to a temperature induced transition from twinning to slip. However, Zheng et al. [18] observe that $\langle 110 \rangle$ Au NWs loaded in tension deform by twinning at room temperature. This is in agreement with the two-parameter model shown in Fig. 5, as well as MD predictions from other groups [51, 57].

Occasionally, the effect of side surfaces can override the predictions based on the Schmid factor, as in the case of Cu $\langle 100 \rangle$ with $\{100\}$ side surfaces in tension [52]. The preference to twinning over f-slip (as predicted by the Schmid factor) has been attributed to the ability of $\{100\}$ surface to orient to $\{111\}$ surface. Nonetheless, it is still surprising that the trailing partial has not been observed for Cu NWs of this geometry [52, 54], even though its Schmid factor is twice of the Schmid factor of the leading partial. This may be caused by the shape of the NW cross section. According to [59], dislocation prefers to nucleate at the NW corner, but has an even stronger preference to be close to the screw orientation (i.e. parallel to the Burgers vector). Therefore, a preferred corner for leading partial nucleation may be an unfavorable site for trailing partial nucleation. More study is needed to understand why the trailing partial fails to nucleate in these NWs.

IV. YIELD STRENGTH

During the last 7 years, there has been significant interest in the compression (and more recently, tension) tests of micro-pillars fabricated using the focused ion beam (FIB) [21]. These experiments have shown that the flow stresses of single crystal micro-pillars increase dramatically as their diameters decrease from $10 \mu\text{m}$ to 100 nm . This naturally raises the question: how does the yield strength depend on diameter for nano-pillars or nanowires with diameters less than 100 nm ? While the experimental data for NWs is starting to emerge [17, 18, 60, 61], computer simulations have been applied extensively to predict the strength of NWs. In this section, we review the current understanding of the strength of metal NWs based on computer simulations and theoretical models.

Fig. 6(a) shows representative stress-strain curves of FCC NWs of different orientations under uniaxial tension or compression predicted by MD simulations. At small enough strains, the NW remains elastic, i.e. the stress-strain curve is completely reversible. The stress-strain curve is a smooth (potentially non-linear) function in the elastic regime. Beyond a critical strain, the stress drops abruptly and the stress-strain curve becomes irreversible upon unloading. The stress at this critical condition is called the yield stress (or yield strength) σ_Y .

MD simulations have predicted that the yield stress of FCC metal NWs depends on the orientation and size of the NWs, the type of loading (tension versus compression), strain rate,

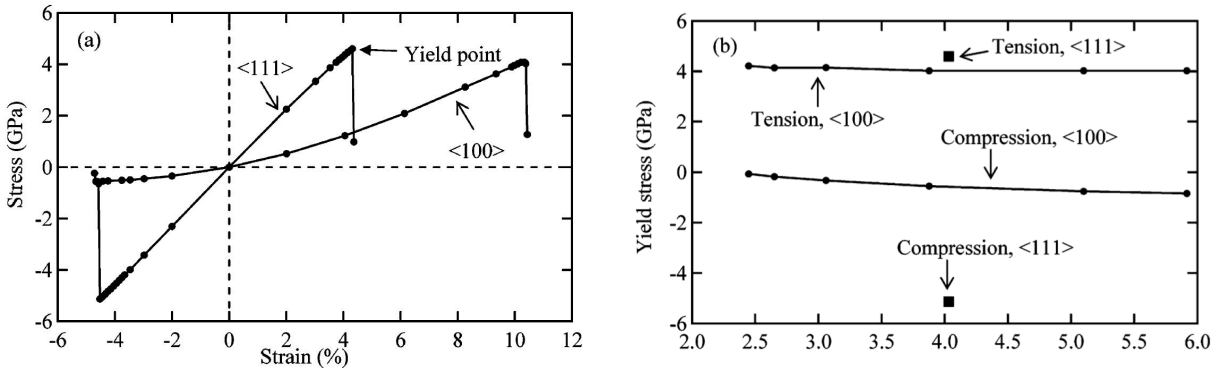


FIG. 6: (a) Uniaxial tensile and compressive stress-strain curves for FCC Au NWs oriented along $\langle 111 \rangle$ and $\langle 100 \rangle$ orientations with square ($4 \text{ nm} \times 4 \text{ nm}$) cross section. (b) The yield stress of $\langle 100 \rangle$ and $\langle 111 \rangle$ Au NWs with square cross sections as a function of their size. (Reprinted with permission from [62].)

and temperature. However, in bulk FCC metals, the yield stress is approximately symmetric, weakly strain rate dependent and the yield stress divided by the Young's modulus is nearly independent of temperature [63]. The following is a summary of the observations from MD simulations on the yield stress of FCC metal NWs.

- The yield stress depends on NW orientation and whether the NW is loaded in tension or compression (see Fig. 6(b)). For example, the magnitudes of the yield strength for a 6 nm thick Au $\langle 100 \rangle$ NW in tension and compression are different by more than a factor of 4. The three most studied orientations are $\langle 100 \rangle$, $\langle 110 \rangle$, and $\langle 111 \rangle$ [55, 62].
- The yield stress varies with NW width d . A behavior of the form of $\sigma_Y = \sigma_Y^\infty + K d^{-1}$ is often observed, where σ_Y^∞ and K are independent of d [56, 62].
- The yield stress strongly depends on the shape of the NW cross section. For example, the yield stress at 300 K of Cu $\langle 111 \rangle$ NWs is about 10 GPa for circular cross sections but only about 6.5 GPa for square cross sections [53].
- The yield stress decreases with increasing temperature [44, 53, 55]. The temperature dependence has been observed to follow two trends: $\sigma_Y = \sigma_0 - A T$ and $\sigma_Y = \sigma_0 - A \sqrt{T}$ depending on the interatomic potential model. The strength reduction with temperature can be as much as 50% from 0 K to 500 K.

There is a general consensus that FCC NWs (both in experiments and MD simulations) should be free of dislocations before loading, such that yielding is controlled by dislocation nucleation from the surface. In other words, the NWs are in a “dislocation-starved” state [30]. Therefore, the dependence of yield strength on geometry, loading type, strain rate, and temperature should be understood in terms of the critical condition for dislocation nucleation. In the following, the behavior of yield strength is rationalized in terms of Schmid factor, surface stress, and nucleation rate theories. Alternative nucleation or yield criteria that have been proposed in the literature are discussed afterwards. However, the only theory that can explain all of the MD observations that are potentially relevant at experimental strain rates is classical nucleation theory.

A. Effect of Schmid factor and surface stress

The first nucleation event upon yielding, in all existing MD simulations, is the nucleation of the leading partial. This event is the rate limiting step that determines the yield strength [53, 62]. Hence, the variation of the Schmid factor of the leading partial with NW orientation and loading type, as listed in Table III, naturally contributes to the dependence of the yield strength on these two parameters. This suggests that the critical resolved shear stress (CRSS), which is the yield stress multiplied by the Schmid factor of the leading partial, may be a better criterion for yielding than the normal stress along the NW axis.

As discussed in Section II, the surface stress induces a compressive stress at the interior of the NW in the absence of the applied load. As a result, the stress at the interior of the NW is different from the applied stress. Taking into account the effects from both the Schmid factor and the surface stress, Fig. 7 plots the CRSS at the interior of the NW at the onset of yielding [53]. The dependence on NW width is now almost completely removed, showing that the surface stress is the dominant cause of the size dependence. The tension-compression asymmetry in Fig. 7 is also significantly reduced compared with Fig. 6(b). This shows that the Schmid factor of the leading partial and the surface stress are the primary causes of the tension-compression asymmetry.

While the Schmid factor and surface stress explanations have proved to be very useful, certain observations in the MD simulations still remain puzzling. First, it is not clear why the yield strength of Au $\langle 100 \rangle$ NWs in tension have a much weaker size dependence than

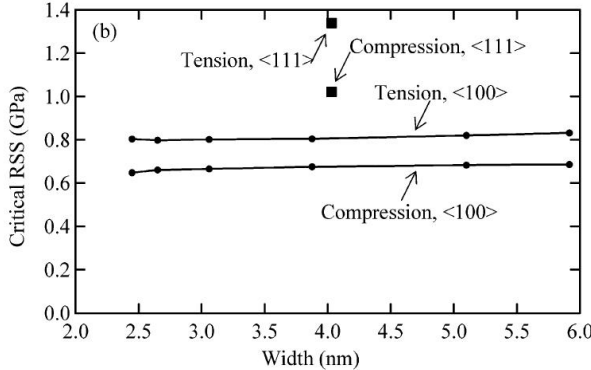


FIG. 7: The resolved shear stress on the interior of a Au NW at yielding. (Reprinted with permission from [62].)

in compression (see Fig. 6(b)) [62]. Second, there still exists an un-explained orientation dependence and tension-compression asymmetry, as shown in Fig. 7, even after both the Schmid factor and surface stress effects have been factored out. These behaviors may be caused by rearrangement and energetics of the surface atoms during dislocation nucleation.

B. Classical nucleation theory

Classical nucleation theory (CNT) [64–69] provides an appropriate framework to discuss the dislocation nucleation rate and hence the yield strength of NWs. According to CNT, the dislocation nucleation rate under stress σ and temperature T is given by the following expression,

$$I(\sigma, T) = N_s \nu_0 \exp \left[-\frac{G_c(\sigma, T)}{k_B T} \right] \quad (5)$$

where N_s is the number of equivalent nucleation sites, ν_0 is a frequency prefactor, G_c is the activation Gibbs free energy for dislocation nucleation, and k_B is Boltzmann's constant. The Becker-Döring theory [64] gives an explicit expression for ν_0 , which can be computed by atomistic simulations [68, 69]. ν_0 is often approximated by the Debye frequency ν_D of the crystal, which is typically on the order of 10^{13} s^{-1} .

Roughly speaking, the yield strength σ_Y of the NW is the stress at which the dislocation nucleation rate reaches a threshold value, i.e. $I(\sigma_Y, T) = I_{\text{th}}$. The threshold nucleation rate, I_{th} , is the inverse of the characteristic time in which the NW is subjected to stress σ_Y . For constant strain rate experiments and simulations, I_{th} is on the order of the strain rate, which

is about 10^8 s^{-1} for MD simulations and 10^{-3} s^{-1} for experiments.

Eq. (5) shows that the nucleation rate is very sensitive to the activation Gibbs free energy $G_c(\sigma, T)$. For a given T , $G_c(\sigma, T)$ usually decreases rapidly with σ , so that the nucleation rate $I(\sigma, T)$ is very sensitive function to stress. The activation volume, defined as:

$$\Omega(\sigma, T) \equiv -\frac{\partial G_c(\sigma, T)}{\partial \sigma} \Big|_T \quad (6)$$

measures the sensitivity of $G_c(\sigma, T)$ to the applied stress σ and is approximately the magnitude of the Burgers vector times the area enclosed by the critical dislocation loop for dislocation nucleation [69].

The following implicit equation for the yield strength σ_Y has been derived [67, 70] by considering a scenario in which the NW is loaded at a constant strain rate $\dot{\epsilon}$.

$$\frac{G_c(\sigma_Y, T)}{k_B T} = \ln \frac{k_B T N_s \nu_0}{E \dot{\epsilon} \Omega(\sigma_Y, T)} \quad (7)$$

This equation is derived based on the assumption that the NW remains linear elastic with Young's modulus E prior to yielding and that ν_0 is insensitive to σ and T . These are reasonable assumptions for the experimental conditions, although the NWs usually become non-linear elastic prior to yielding in many MD simulations.

By numerically solving Eq. (7), we can predict the yield strength σ_Y , provided with the knowledge of the activation Gibbs free energy $G_c(\sigma, T)$ and reasonable estimates of N_s and ν_0 . $G_c(\sigma, T = 0)$ can be determined from zero temperature chain-of-states methods, such as the nudged elastic band [71] and string [72] methods, directly applied to atomistic models. Alternatively, continuum models can be used, but the accuracy of these models are limited by the approximation introduced at the dislocation core. Finally, the temperature dependence of $G_c(\sigma, T)$ has been approximated using the thermodynamic compensation law (or Meyer-Neldel Rule) [67], as well as determined numerically by umbrella sampling [68, 69].

The yield stress predicted by Eq. (7) has several generic features that are in agreement with the observations from MD simulations. These agreements support the point of view that the yield strength of NWs can be understood by properly applying classical nucleation theory to dislocation nucleation from the NW surface.

The first evidence from MD simulations in support of CNT is the dramatic decrease of yield strength as the NW cross section changes from a circle to a square [53, 59]. The dislocation nucleus in a square pillar will have, in general, a shorter line length than in

circular pillars leading to a lower G_c and σ_Y [59]. Additionally, square cross-sections may induce a stress concentration due to the surface stress [53] which further enhances nucleation from the corners.

Another piece of strong evidence in support of CNT is the reduction of yield strength with increasing temperature [53, 55]. This is a consequence of the thermally activated nature of the dislocation nucleation process and is naturally obtained when Eq. (7) is solved numerically. The strong temperature dependence of the yield strength is consistent with a relatively small activation volume (compared with, e.g. forest cutting mechanisms in the bulk [73]) of the dislocation nucleation process under the high stress conditions of these MD simulations.

The CNT approach also makes other interesting predictions concerning the yield strength of NWs under experimental conditions. First, the yield strength is predicted to depend on the applied strain rate $\dot{\epsilon}$, which is explicitly included in Eq. (7). The reduction of strain rate from MD values, on the order of 10^8 s^{-1} , to experimental values, on the order of 10^{-3} s^{-1} , can lower the yield strength by several hundred MPa's [67, 68]. This allows extrapolation of MD results to predict NW yield strength at experimental conditions.

Second, Eq. (7) predicts a dependence of NW yield strength on NW size, through the number of nucleation sites N_s . A thicker (or longer) NW has more nucleation sites than a thinner (or shorter) NW and will have a somewhat lower yield strength. However, this effect only leads to a logarithmic dependence of σ_Y on the NW width d , and is much weaker than the $1/d$ dependence arising from the surface stress effect (Section IV A). Hence, the dominant mechanism for the size effect of yield strength for FCC metal NWs is the surface stress.

C. Alternative nucleation criteria

In the previous subsection, we presented the view point that the yield strength of NWs can be understood through classical nucleation theory, in terms of the activation free energy G_c for dislocation nucleation as a function of the applied stress σ and temperature T . However, there have been several reports suggesting the need for an alternative approach. For example, Zepeda-Ruiz et al. [56] proposed that the local stress in the surface layer instead of the applied stress should be used as a yield criterion. Cao and Ma [53] proposed the local

shear strain on surface atoms as a yield criterion. Park and Zimmerman [44] suggested that the strengthening is caused by changes in dislocation drag. Both Rabkin et al. [55] and Marian and Knapp [74] have suggested buckling as an important event prior to dislocation nucleation. Rabkin et al. [55] have also proposed a strain based nucleation criterion that accounts for the temperature induced strain fluctuation. In this section, we discuss these approaches and show that they are either consistent with the CNT based approach, or are unlikely to influence the NW yield strength at the experimental strain rates.

In their study of Au $\langle 100 \rangle$ NWs under compression, Zepeda-Ruiz et al. [56] claim that the applied stress σ is not the controlling factor for dislocation nucleation, because, interestingly, the applied stress actually drops (at low temperatures) prior to dislocation nucleation. To explain their observations, the authors propose that the local stress in the surface layer atoms (terraces) should be used as the nucleation criteria. The authors note that during compression the $\{110\}$ terraces experience higher stresses than the $\{100\}$ terraces, and this fact correlates with the observation of preferred nucleation sites on the $\{110\}$ terraces. However, unlike the Virial stress which is well defined as the average stress over the entire simulation cell, there is no unique definition for the local stress of a small group of atoms [75]. It is not clear whether the rapid increase of the local (compressive) stress on $\{110\}$ facets prior to yielding is a consequence of the specific choice of local stress definition used in the analysis. In addition, while the above observation is important for understanding how the NWs yield in MD simulations, it is likely that at the experimental strain rate the NWs will nucleate dislocations under much lower stresses, up to which the NWs are still linear elastic.

To analyze their MD simulations of Cu NWs, Cao and Ma [53] introduced the notion of local strain shear invariant (SSI), which measures the amount of shear deformation around each atom. They observe that in both NWs with square cross sections and NWs with circular cross sections, dislocation nucleation occurs when certain atoms have their SSI exceeding a threshold value of 0.085. Despite this correlation, it is not clear how the SSI parameter can explain temperature or strain rate dependence of the yield strength. As mentioned above, at experimental time scales, metal NWs are likely to remain linear elastic prior to yielding such that the resolved shear strain (proposed in [53]) and resolved shear stress (used in [62]) are proportional to each other.

Park and Zimmerman [44] suggested that phonon drag has an effect on the strength of NWs and explains the strain rate dependence of yield strain. While phonon drag has been

shown to be size dependent below 40 nm [76], it is unlikely to be important in nucleation since phonon drag only relates to the motion of the dislocations after they are nucleated. The change in yield strength with strain rate observed in these MD simulations can be fully explained by CNT through Eq. (7), and the size dependence can be explained through the surface stress.

In their simulations of Au NWs in compression, Rabkin et al. [55] observed a number of cases in which dislocation nucleation is preceded by a buckling instability of the NW. This behavior is observed in $\langle 100 \rangle$ and $\langle 110 \rangle$ NWs when certain interatomic potentials are used but not in $\langle 111 \rangle$ NWs. However, it is reasonable to expect that at experimental time scales dislocation nucleation will occur at much lower stresses and will not be driven by elastic buckling (for nanopillars of the aspect ratio in [55]). The same argument applies to the surface wrinkling observed by Marian and Knap [74] in the compression simulations of Au $\langle 100 \rangle$ nano-pillars using the quasi-continuum method.

In the cases where dislocation nucleation is not preceded by an elastic instability (e.g. for $\langle 111 \rangle$ NWs), Rabkin et al. [55] proposed a strain-based dislocation nucleation criterion to explain the temperature dependence of the yield strength, in the spirit of the Lindemann criterion for melting [77]. First, the authors defined a “thermal strain”, $\epsilon_{\text{therm}} \equiv \langle \Delta r \rangle / a$, where $\langle \Delta r \rangle$ is the average distance of an atom from its equilibrium position, and a is the equilibrium lattice constant. Second, the authors found that, under zero applied stress, ϵ_{therm} increases with T for both surface and bulk atoms, in the form of either $A\sqrt{T}$ or AT , depending on the interatomic potential. Third, the temperature dependence of the NW yield stress (when yield is not controlled by elastic buckling) can be well described by the empirical relation,

$$\sigma_Y(T) = E(T) [\epsilon_c - \epsilon_{\text{therm}}(T)] \quad (8)$$

where E is the Young’s modulus and ϵ_c is an empirical constant. While Eq. (8) seems to agree well with their MD observations, it is not clear how this heuristic relationship can be explained except through classical nucleation theory, which not only captures the temperature dependence, but also geometric and strain rate effects.

V. PHASE TRANSFORMATION

In addition to slip and twinning, both of which are controlled by the nucleation of lattice dislocations, phase transformations between the FCC and the BCT (body-centered tetragonal) have been predicted as an alternative plastic deformation mechanism for very thin $\langle 100 \rangle$ FCC metal NWs [78–80]. In the existing studies, the FCC-BCT phase transformation occurs spontaneously under zero applied load, leading to contraction of the NW length, and is entirely driven by the surface stress. Intermetallic Ni-Al [81] and Cu-Zr [82] NWs with initial B2 phase have been shown to undergo reversible transformations between the B2 and BCT phases during tensile loading and unloading, which leads to a pseudo-elastic behavior to be discussed in the next section.

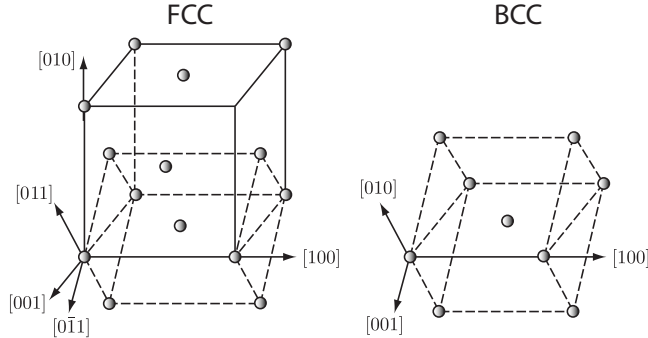


FIG. 8: Bain path transforming FCC structure to BCC structure.

To understand the FCC-BCT phase transformation, one must first consider the *Bain path* [83, 84]. Along the Bain path, a bulk FCC crystal can homogeneously transform into a BCC (body-centered cubic) structure. This is achieved by contracting along the $[100]$ direction and simultaneously expanding along the $[010]$ and $[001]$ directions of the FCC structure. When the length along the $[100]$ direction becomes a factor of $\sqrt{2}$ of the lengths along the $[010]$ and $[001]$ directions, the distorted FCC structure becomes a BCC structure, as shown in Fig. 8. The $[010]$ and $[001]$ directions of the BCC structure corresponds to the $[011]$ and $[0\bar{1}1]$ directions of the original FCC structure. However, if the transformation along the Bain path does not stop at the exact proportion given above, the result is a BCT structure. BCT is a distorted BCC structure, i.e. the length along the new $[100]$ direction is not the same as those along the new $[010]$ and $[001]$ directions.

The FCC-BCT transformation does not occur homogeneously over the entire NW. Instead, the transformation is initiated at the two ends and proceeds by propagating the two $\langle 100 \rangle$ phase boundaries towards each other along the NW axis [78]. Therefore, the FCC-BCT phase transformation also occurs in a layer-by-layer fashion, as in twinning. The B2-BCT phase transformation predicted for Cu-Zr NWs [82] also proceeds by the propagation of $\langle 100 \rangle$ phase boundaries, which are normal to the NW axis. However, the B2-BCT phase transformation predicted for Ni-Al NWs [81] proceeds by the propagation of $\{101\}$ phase boundaries, which are inclined to the NW axis, making the transformation mechanism more similar to twinning discussed in previous sections.

MD simulations using the Au MEAM potential predict that the FCC-BCT phase transformation only occurs in a narrow range of NW diameters [38, 78]. Au $\langle 100 \rangle$ NWs with cross section area larger than 4 nm^2 relaxes by reorientation into FCC $\langle 110 \rangle$ NWs through twinning, as discussed earlier. In contrast, all Au EAM potentials predict $\langle 100 \rangle$ -to- $\langle 110 \rangle$ reorientation instead of FCC-BCT phase transformation for all NW diameters. *Ab-initio* methods (DFT and TB) have been used to study the FCC-BCT phase transformation as well [79, 80]. The result show that all BCT phases are unstable in the bulk, however, the surface stresses in NWs can stabilize the Au and Pt BCT phases. Nonetheless, the BCT $\langle 100 \rangle$ NW structure is always higher in energy than the reoriented FCC $\langle 110 \rangle$ NW. Therefore, at the experimental time scales, the BCT NW may be very short-lived before it spontaneously transforms to the reoriented FCC structure. In this case, the BCT structure acts as an intermediate step for the $\langle 100 \rangle$ -to- $\langle 110 \rangle$ reorientation transformation, as observed in some simulations [80].

Recently, Zheng et al. [18] have shown that some nanocrystals appear to change phase or reorient after fracture. The authors believe that the final phase is BCT Au. However, the evidence is not conclusive since the imaging is based on a single two-dimensional image. It is reasonable to expect phase transformation to be a viable deformation mechanism in other types of metal NWs, such as intermetallic NWs [81, 82].

VI. PSEUDO-ELASTIC AND SHAPE MEMORY EFFECTS

Pseudo-elastic and shape memory effects are two closely related phenomenon in which materials deform reversibly to very high (e.g. 10%) strains. In the pseudo-elastic effect, the

sample recovers its original shape as soon as the load is removed. In the shape memory effect, heating is required for shape recovery after the load is removed. This surprising behavior can appear when deformation is caused by moving interfaces between different crystalline phases or twins [85–88]. In bulk samples, the pseudo-elastic and shape-memory effects have been found in alloys (e.g. Cu-Zn, Ni-Ti), but not in single-component metals. However, both the pseudo-elastic and shape-memory effects have been predicted to occur in single-component FCC metal NWs due to the strong surface stress effects at the nanoscale.

MD simulations have shown that, under compression, FCC $\langle 100 \rangle$ NWs with $\{100\}$ side surfaces transform into $\langle 110 \rangle$ NWs with $\{111\}$ side surfaces by twinning [38, 46, 57, 89, 90]. Under tension, the reverse transformation occurs also by the same twinning mechanism. This transformation between the two FCC NW structures has been called reorientation. When the NW is sufficiently thin, the surface stress alone can induce reorientation from the $\langle 100 \rangle$ direction to the $\langle 110 \rangle$ direction in the absence of an applied load [46, 57, 89, 90]. The resulting $\langle 110 \rangle$ NW can transform to the $\langle 100 \rangle$ orientation when a sufficiently large tensile load is applied. As soon as the load is removed, however, the surface stress spontaneously transforms the NWs back to the $\langle 110 \rangle$ orientation. The maximum reversible strain of this reversible transformation can be estimated as $\sqrt{2} - 1 = 41.4\%$, leading to a very large pseudo-elastic effect.

For slightly thicker FCC $\langle 100 \rangle$ NWs, the surface stress alone is not sufficient to initiate twinning and cause reorientation at room temperature, but this reorientation can occur at elevated temperatures. In this case, after the FCC $\langle 110 \rangle$ NW reorients to the $\langle 100 \rangle$ direction under tension, the structure remains meta-stable even after the load is removed. The NW returns to the $\langle 110 \rangle$ orientation when it is heated to a higher temperature, leading to a shape memory effect. The existence of a critical temperature to initiate the $\langle 100 \rangle$ -to- $\langle 110 \rangle$ reorientation is caused by the presence of a free energy barrier for the first partial dislocation to nucleate from the NW surface. After the first nucleation event, the nucleation barriers of subsequent partial dislocations on adjacent $\{111\}$ planes are apparently lower, resulting in continued propagation of the twin and thus reorientation of the NW. The $\langle 110 \rangle$ oriented NW is always in a lower energy state than the $\langle 100 \rangle$ oriented NW because the $\langle 110 \rangle$ oriented NW has a smaller total surface area as well as a lower surface energy per unit area. Hence it is reasonable to expect the $\langle 100 \rangle$ -to- $\langle 110 \rangle$ reorientation to occur given sufficient assistance from thermal fluctuation.

The ability of FCC NWs to exhibit shape memory and psuedo-elastic effects depends on both the material as well as the interatomic potentials models. For example, using EAM potentials, Liang and Zhu predict [46] that Cu exhibits both pseudo-elastic and shape memory effects, Ni shows pseudo-elastic effects, Au exhibits pseudo-elastic effect at very low temperatures, and Al does not show either pseudo-elastic or shape memory effect at all. Park et al. [57] showed that Cu, Ni and Au NWs all show both pseudo-elastic and shape memory effects with different critical temperatures. The different predictions for Ni are most likely caused by the difference in the interatomic potentials, causing different surface stresses and energy barriers to dislocation nucleation.

The tendency for NWs to exhibit pseudo-elastic and shape memory effects is controlled by the competition between twinning and slip, which is discussed in Section III. Al has the lowest twinnability of the material studied and $\langle 110 \rangle$ NWs fail via f-slip (see Fig. 5) and thus exhibit no pseudo-elastic or shape memory effects. Au has the next lowest twinnability and pseudo-elastic only at low temperatures. Cu and Ni show transitions between pseudo-elastic and shape memory effects that are size and temperature dependent.

MD simulations [78–80] using the MEAM potential have predicted that Au $\langle 100 \rangle$ NWs can spontaneously undergo FCC-BCT phase transformation driven by the surface stress (see Section V). If the BCT phase can transform back to the FCC $\langle 100 \rangle$ NW structure under tension, then the result is a pseudo-elastic or shape memory effect, via the phase transformation instead of the reorientation mechanism. However, this possibility has not yet been investigated by MD simulations. A similar mechanism, the B2-BCT phase transformation, has indeed been found to lead to the pseudo-elastic and shape memory effects for intermetallic Ni-Al [81] and Cu-Zr [82] NWs.

The possibility of pseudo-elastic and shape memory effects for FCC NWs has not been studied for $\langle 100 \rangle$ NWs with cylindrical side surfaces, even though these NWs have been predicted to twin and reorient to the $\langle 110 \rangle$ direction under compression [55]. This possibility seems likely given that reoriented $\langle 110 \rangle$ NWs should have a lower energy than $\langle 100 \rangle$ NWs.

Recent experiments have validated the predicted reorientation in Au NWs with diameters of 40–150 μm [60]. The NWs are initially along $\langle 110 \rangle$ direction with atomically smooth $\{111\}$ side surfaces and rhombic cross sections. Twins are nucleated at 1.5 GPa axial stress, and propagate through the NWs to reorient them. The reoriented NWs are along $\langle 100 \rangle$ direction with $\{100\}$ side surfaces and rectangular cross sections. This remarkable validation suggests

that MD simulations, even though limited to high strain rate conditions, have the potential to be predictive for deformation mechanisms at the experimental strain rate.

VII. BENDING AND TORSION

The previous four sections have primarily dealt with plasticity of FCC NWs under uniaxial loading. Given the complexity of deformation behavior already observed in MD simulations and the difficulty of conducting nanoscale experiments, it is understandable that so much attention has been focused on the simple uniaxial loading condition. In this section, we discuss some of the simulations [91–96] of the bending and torsion of metal NWs. One of the unique opportunities in studying NWs in bending and torsion is that these loading conditions provide the opportunity to study the effects of strain gradients on NW plasticity. Strain gradients imposed by the loading condition lead to geometrically necessary dislocations (GND) that accommodate a plastic twist or curvature [97]. Due to GND’s, NWs are no longer dislocation starved, leading to a different realm of plastic behaviors.

A. Bending

Zheng et al. [91, 92] have conducted MD simulations of the bending of $\langle 100 \rangle$ oriented Cu NWs. The NWs have square cross section and are initially defect free. The plastic deformation is dominated by p-slip and twinning, not unlike the deformation of Cu NWs under uniaxial loading. Furthermore, plasticity is always initiated from the compressive side of the $\langle 100 \rangle$ NW. This is consistent with fact that the leading partial has a higher Schmid factor when a $\langle 100 \rangle$ NW is in compression than in tension, as listed in Table III. At a later stage of deformation, fivefold deformation twin structures are commonly observed in these bending simulations.

In a related study, Csikor et al. [93] have used a continuum model of the statistics of dislocation avalanches to predict that deformation in bent wires transitions from diffuse to localized as the wire diameter reduces from millimeters to a micron. This suggests that in bent NWs, the plastic deformation should be completely localized. However, the statistical nature of dislocation avalanches is not necessarily the same as that of dislocation nucleation, which controls NW plasticity. Because NW orientation plays a significant role in dislocation

nucleation under uniaxial loading, it would be interesting to see if and how NW plasticity in bending depends on NW orientation from atomistic simulations.

B. Torsion

The torsion of Au and Al NWs has been studied using both MD and dislocation dynamics [94–96]. The authors investigate the size and orientation dependent plasticity which included three high symmetry orientations: the $\langle 100 \rangle$, $\langle 110 \rangle$ and $\langle 111 \rangle$. For $\langle 111 \rangle$ and $\langle 100 \rangle$ orientations, low angle twist boundaries are observed to form on the (111) and (100) planes perpendicular to the wire axis by the nucleation and organization of perfect dislocations on their $\{111\}$ slip planes as shown in Fig. 9(a)-(b). Continued plasticity occurs at this boundary as it evolves into a high angle grain boundary localizing the plastic deformation.

The $\langle 110 \rangle$ NWs accommodate the plastic twist in a very different way from $\langle 111 \rangle$ and $\langle 100 \rangle$ NWs. The dislocations that nucleate are parallel to the NW axis on $\{111\}$ slip planes that are also parallel to the axis. Fig. 9 (c) shows that the first few nucleation events in Au NWs give rise to the leading partial dislocations with Burgers vectors of the $\frac{a}{6}\langle 112 \rangle$ type. For Au NWs below 15 nm in diameter, these are the only types of dislocations observed. However, in Al NWs of all diameters and some Au NWs, the trailing partial dislocation quickly follows and the NW is filled with perfect screw dislocations. An example of perfect dislocations in Al NWs is shown in Fig. 9 (d).

A screw dislocation lying along the axis of a wire was originally studied by Eshelby [98] in which he considered the screw dislocation as a grown-in defect in whiskers. The twist caused by such a dislocation is now termed the Eshelby twist. The MD simulations discussed above predict that the Eshelby twist involving screw dislocations along the wire axis can be a deformation mechanism for metallic NWs or whiskers.

C. Pseudo-elasticity of $\langle 110 \rangle$ NWs

The unique deformation mechanisms of $\langle 110 \rangle$ NWs in torsion gives rise to a pseudo-elastic effect and potentially a shape memory effect [94, 95]. As noted above, when FCC $\langle 110 \rangle$ NWs are subjected to torsion, dislocations parallel to the NW axis are nucleated. For Au NWs of 15 nm diameter and below, only leading partials are nucleated, while Al NWs

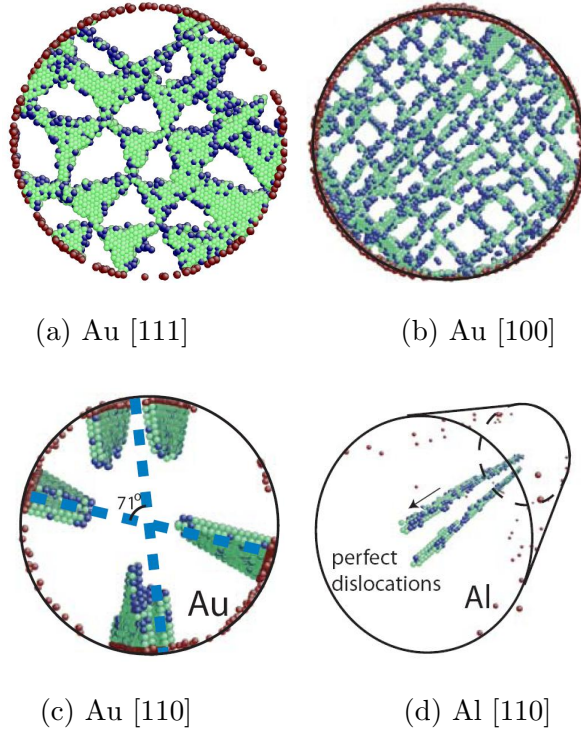


FIG. 9: Dislocation structure of FCC metal (Au and Al) NWs of different orientations subjected to torsion. (Reprinted with permission from [94] and [95].)

always nucleate perfect dislocations. This mechanistic difference leads to different types of torque-twist curves for 5 nm diameter Au and Al NWs. When a Au NW is unloaded, the twist angle returns to zero when the applied torque drops to zero, exhibiting a pseudo-elastic behavior, as defined in Section VI. This is because the partial dislocations parallel to the NW axis are unstable in the absence of applied torque. They are pulled out of the NW by the stacking faults. In comparison, when the Al NW is unloaded, a non-zero twist angle persists even when the applied torque drops to zero, which signifies irreversible plasticity. Continuum analysis confirms that multiple perfect screw dislocations are meta-stable inside an elastic cylinder [95, 96], as in the case of Al NWs. However, a NW containing screw dislocations parallel to its axis has a higher energy than a defect-free NW. Hence it is possible that these screw dislocations can leave the NW at an elevated temperature, giving rise to a shape-memory effect. This possibility has not yet been studied by MD simulations or experiments.

VIII. BCC METAL NANOWIRES

MD simulations of metal NWs have been primarily focused on FCC metals, such as Cu, Ni, Au, and Al. There have been relatively few simulations of metal NWs with other crystal structures, such as Fe, W and Mo, which have the body-centered cubic (BCC) structure, or Ti and Mg, which have the hexagonal closed packed (HCP) structure. One reason for this dominance of FCC metals is that, even in the bulk, the plasticity of BCC metals is not as well understood as that of FCC metals.

In FCC metals, strength is governed by the ability of dislocations to break away from pinning points created by particles or other dislocations. In BCC metals, the intrinsic lattice resistance also plays an important role in controlling the plastic response. The non-planar compact core structure of the screw dislocations gives rise to strong temperature and strain rate sensitivity of the yield strength because thermal activation is required for screw dislocation motion [99, 100].

The different dislocation properties in FCC and BCC metals must have an impact on the plasticity of metal NWs. Because dislocations have a planar core structure and a high mobility in FCC metals, it is reasonable to expect that all mobile dislocations can easily escape the NW, leaving it in a “dislocation-starved” state [30]. In this case, NW plasticity is dominated by dislocation nucleation from the surface. In contrast, molecular dynamics and dislocation dynamics simulations have shown that in a BCC NW dislocations may not leave the NW so easily [101, 102]. Instead, they may multiply and generate more dislocations under suitable stress conditions. As a result, BCC NWs may not be in a dislocation starved state, at least during plastic deformation, so that the yield stress and flow stress of BCC NWs may need to be understood using a different approach than that for FCC NWs.

A possible multiplication mechanism in BCC metals [101] is shown in Fig. 10. In this simulation, an initially mixed dislocation is placed in a NW under constant compressive stress. The dislocation spontaneously reorients to a screw dislocation. As the dislocation advances, a cusp forms and evolves into a loop, which transforms the single dislocation into three dislocations. This mechanism is able to operate again as long as the stress is above the critical stress required to expand the loop.

It has been very difficult to verify the predicted dislocation multiplication mechanism in BCC nano-pillars by experiments. Compression tests indeed reveal different size depen-

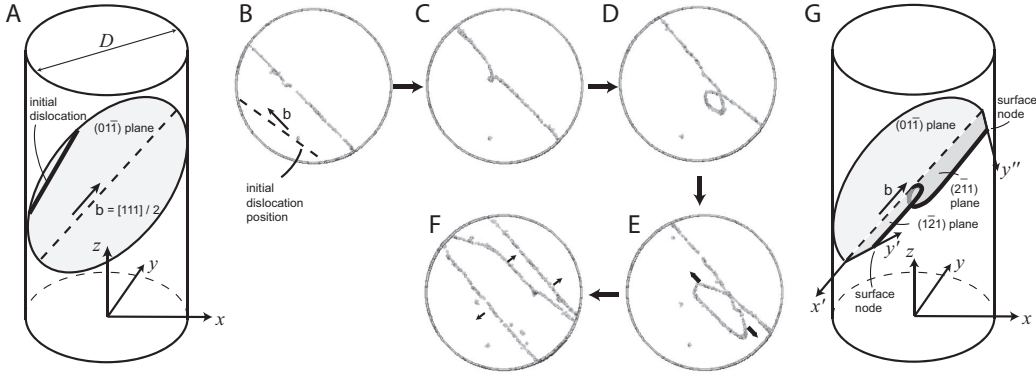


FIG. 10: The evolution of single dislocation in a BCC Mo NW under compressive stress of 9 GPa.
(Reprinted with permission from [101])

dence of the yield strength in FCC and BCC micro-pillars [20, 21]. However, this can be explained by the high lattice resistance of the screw dislocations in BCC metals, and may not necessarily be a signature of the self-multiplication mechanism. While it is generally believed that FCC pillars thinner than 100 nm in diameter should be dislocation starved, recent *in situ* TEM observations in BCC Mo nano-pillars of the same diameter have revealed many dislocation lines prior to deformation [103]. It would be interesting to see if the flow strength of these BCC nano-pillars is determined by these pre-existing dislocations or by new dislocations nucleated from the surface.

IX. SUMMARY AND OUTLOOK

In many nanostructures, including FCC metal NWs, dislocation nucleation is an important process that governs strength, mechanisms of plasticity, ductility as well as shape memory and pseudo-elastic effects. Dislocation nucleation, at least in the experimental strain rate, can be well described by classical nucleation theory (CNT) which predicts strong shape and temperature effects on the yield strength, as well as a weak strain rate dependence. A simple model can be constructed, based on the Schmid factor and the generalized stacking fault energies, to predict whether FCC NWs under uniaxial loading will yield by slip via perfect dislocations, slip via partial dislocations, or twinning. However, the competition between these mechanisms under experimental conditions can be significantly influenced by

local surface features.

The surface stress becomes an important effect at the nanoscale and is a major cause of the size dependence of yield strength. It also gives rise to unique pseudo-elastic effects and shape memory effects, by triggering reorientation from $\langle 100 \rangle$ to $\langle 110 \rangle$ in FCC NWs, or phase transformation in intermetallic NWs. Because pseudo-elastic and shape memory effects can be exploited in novel NEMS devices, it is significant that these predictions have been verified by experiments.

Other loading modes, such as bending and torsion, have been less studied by atomistic simulations but hold significant interest. The torsion of properly oriented single crystal wires show promise for shape memory and pseudo-elastic effects. It would be interesting to explore similar effects for metal NWs in bending, which could lead to reversibly foldable nano-structures. More simulations and experiments on BCC, HCP and intermetallic NWs can provide further insights on the plasticity mechanisms at the nanoscale.

The most pressing need in NW mechanics research today is to establish a quantitative connection between atomistic simulations and experiments. One challenge is to reduce the large scatter in the experimental data in the Young's modulus [104] and yield strength measurements. A promising approach is to focus on NW samples synthesized from those methods that guarantee a high degree of perfection and repeatability both inside the NWs and on the surface. Since even these NWs inevitably have some surface roughness, a systematic study of the surface roughness in atomistic simulations is still needed.

Two important challenges for modelling are presented by the inaccuracy of empirical interatomic potentials and the limited time scale of MD. A promising way to address both problems is to develop an accurate continuum model for dislocation nucleation rate based on CNT and GSF energies. First, this continuum model can take the GSF energies computed by an empirical potential as input, and its predictions can be benchmarked against an explicit atomistic calculation [59, 105]. Then the continuum model can take the GSF energies computed by more accurate first-principles methods as input, and make predictions that are not limited by the accuracy of empirical interatomic potentials. The dislocation rate predictions based on CNT can be first benchmarked against explicit MD simulations at the high temperature or high stress regime [67, 68], after which reliable predictions can be made at the experimental time scales. For NWs under bending and torsion, both molecular dynamics and dislocation dynamics simulations can be used to model the structural evolu-

tion of geometrically necessary dislocations. The crosschecking between atomistic models, continuum models, and experiments will establish a confidence that the essential physics governing NW plasticity is properly understood.

A longer term goal of nanoscale mechanics research is to be able to predict the reliability and failure mode of metal NWs in an actual NEMS device. For example, in a switching device using a NW cantilever, the electric discharge between the NW and the electrode can cause ablation or plastic deformation close to the contact region. Defect generation from plastic deformation can also affect the electrical resistivity or the magnetic properties of metal NWs. The existing atomistic models will need to be extended to incorporate the new physics in these phenomena.

Acknowledgments

This research was supported in part by an appointment to the Sandia National Laboratories Truman Fellowship in National Security Science and Engineering, sponsored by Sandia Corporation (a wholly owned subsidiary of Lockheed Martin Corporation) as Operator of Sandia National Laboratories under its U.S. Department of Energy Contract No. DE-AC04-94AL85000. The work was partly supported by National Science Foundation Career Grant CMS-0547681 and the Army High Performance Computing Research Center at Stanford.

-
- [1] C. M. Lieber, MRS Bulletin **28**, 486 (2003).
 - [2] M. Li, T. S. Mayer, J. A. Siess, C. D. Keating, and R. B. Bhiladvala, Nano Lett. **7**, 3281 (2007).
 - [3] V. P. Menon and C. R. Martin, Anal. Chem. **67**, 1920 (1995).
 - [4] Y. Wu, J. Xiang, C. Yang, W. Lu, and C. M. Lieber, Nature **430**, 61 (2004).
 - [5] T. Whitney, J. Jiang, P. Searson, and C. Chien, Science **261**, 1316 (1993).
 - [6] C. A. Foss, G. L. Hornyak, J. A. Stockert, and C. R. Martin, J. Phys. Chem. **98**, 2963 (1994).
 - [7] W. F. Paxton, K. C. Kistler, C. C. Olmeda, A. Sen, S. K. S. Angelo, Y. Cao, T. E. Mallouk, P. E. Lamment, and V. H. Crespi, J. Am. Chem. Soc. **126**, 13424 (2004).
 - [8] G. A. Ozin, I. Manners, S. Fournier-Bidoz, and A. Arsenault, Advanced Materials **17**, 3011

(2005).

- [9] M. Li, R. B. Bhiladvala, T. J. Morrow, J. A. Siess, K. Lew, J. M. Redwing, C. D. Keating, and T. S. Mayer, *Nature Nanotech.* **3**, 88 (2008).
- [10] Hulteen and C. Martin, *J. Mater. Chem.* **7**, 1075 (1997).
- [11] D. L. Fan, F. Q. Zhu, R. C. Cammarata, and C. L. Chien, *Phys. Rev. Lett.* **94**, 247208 (2005).
- [12] L. Zhang, T. Petit, Y. Lu, B. E. Kratochvil, K. E. Peyer, R. Pei, J. Lou, and B. J. Nelson, *ACS Nano* **4**, 6228 (2010).
- [13] D. Fan, Z. Yin, R. Cheong, F. Q. Zhu, R. C. Cammarata, C. L. Chien, and A. Levchenko, *Nature Nanotech.* **5**, 545 (2010).
- [14] C. Martin, *Science* **266**, 1961 (1994).
- [15] M. Burek and J. Greer, *Nano Lett.* **10**, 69 (2009).
- [16] S. Brenner, *Acta Metal.* **4**, 62 (1956).
- [17] G. Richter, K. Hillerich, D. Gianola, R. Monig, O. Kraft, and C. Volkert, *Nano Lett.* **9**, 3048 (2009).
- [18] H. Zheng, A. Cao, C. R. Weinberger, J. Y. Huang, K. Du, J. Wang, Y. Ma, Y. Xia, and S. X. Mao, *Nature Communications* **1**, 144 (2010).
- [19] Y. Kondo and K. Takayanagi, *Physical Review Letters* **79**, 3455 (1997).
- [20] O. Kraft, P. A. Gruber, R. Monig, and D. Weygand, *Annual Rev. Mater. Res.* **40**, 293 (2010).
- [21] J. Greer and J. de Hosson, *Prog. Mater. Sci.* **56**, 654 (2011).
- [22] A. Cao and Y. Wei, *Physical Review B* **74**, 214108 (2006).
- [23] A. Leach, M. McDowell, and K. Gall, *Advanced functional Materials* **17**, 43 (2007).
- [24] Y. Zhang and H. Huang, *Nanoscale Research Letters* **4**, 34 (2009).
- [25] C. Deng and F. Sansoz, *Nano Lett.* **9**, 1517 (2009).
- [26] F. Sansoz and V. Dupont, *Scripta Mater.* **63**, 1136 (2010).
- [27] C. J. Johnson, E. Dujardin, S. A. Davis, C. J. Murphy, and S. Mann, *J. Mater. Chem.* **12**, 1765 (2002).
- [28] B. Wu, A. Heidelberg, J. J. Boland, J. E. Sader, X. Sun, and Y. Li, *Nano. Lett.* **6**, 468 (2006).
- [29] M. Lucas, A. M. Leach, M. T. McDowell, S. E. Hunyadi, K. Gall, C. J. Murphy, and E. Riedo, *Phys. Rev. B* **77**, 245420 (2008).

- [30] J. Greer and W. Nix, Phys. Rev. B **73**, 245410 (2006).
- [31] W. Tyson and W. Miller, Surf. Sci. **62**, 267 (1977).
- [32] I. Galanakis, N. Papanikolaou, and P. Dederichs, Surf. Sci. **511**, 1 (2002).
- [33] L. Vitos, A. Ruban, H. Skriver, and J. Kollar, Surf. Sci. **411**, 186 (1998).
- [34] F. Boer, R. Boom, W. Mattens, A. Miedema, and A. Niessen, *Cohesion in Metals* (North-Holland, 1988).
- [35] C. Rottman and M. Wortis, Physics Reports **103**, 59 (1984).
- [36] W. D. Nix, *Encyclopedia of Materials: Science and Technology* (Elsevier, 2001), pp. 4136–4141.
- [37] M. E. Gurtin and A. I. Murdoch, Archive of Rational Mechanics and Analysis **57**, 291 (1975).
- [38] J. Diao, K. Gall, and M. Dunn, Physical Review B **70**, 075413 (2004).
- [39] H. Park and P. Klein, Physical Review B **75**, 085408 (2007).
- [40] J. Diao, K. Gall, M. Dunn, and J. Zimmerman, Acta Materialia **54**, 643 (2006).
- [41] V. Vitek, Phil. Mag. **18**, 773 (1968).
- [42] J. Rice, J. Mech. Phys. Solids **40**, 239 (1992).
- [43] J. Hirth and J. Lothe, *Theory of Dislocations* (Krieger, 1982).
- [44] H. S. Park and J. A. Zimmerman, Phys. Rev. B **72**, 054106 (2005).
- [45] E. Tadmor and S. Hai, J. Mech. Phys. Solids **51**, 765 (2003).
- [46] W. Liang and M. Zhou, Physical Review B **73**, 115409 (2006).
- [47] N. Bernstein and E. Tadmor, Phys. Rev. B **69**, 094116 (2004).
- [48] E. Tadmor and N. Bernstein, J. Mech. Phys. Solids **52**, 2507 (2004).
- [49] A. H. Cottrell, *Dislocations and Plastic Flow in Crystals* (Oxford University Press, 1953).
- [50] G. E. Dieter, *Mechanical Metallurgy* (McGraw-Hill, London, 1988).
- [51] H. Park, K. Gall, and J. Zimmerman, J. Mech. Phys. Solids **54**, 1862 (2006).
- [52] C. Ji and H. S. Park, Applied Physics Letters **89**, 181916 (2006).
- [53] A. Cao and E. Ma, Acta Materialia **56**, 4816 (2008).
- [54] W. Liang and M. Zhou, Proceedings of the Institution of Mechanical Engineers, Part C: Journal of Mechanical Engineering Science **218**, 599 (2004).
- [55] E. Rabkin, H. Nam, and D. Srolovitz, Acta Materialia **55**, 2085 (2007).
- [56] L. Zepeda-Ruiz, B. Sadigh, J. Biener, A. Hodge, and A. Hamza, Applied Physics Letters **91**, 101907 (2007).

- [57] H. Park, K. Gall, and J. Zimmerman, Physical Review Letters **95**, 255504 (2005).
- [58] D. H. Warner and W. A. Curtin, Acta Mater. **57**, 4267 (2009).
- [59] C. R. Weinberger, A. T. Jennings, K. Kang, and J. R. Greer, J. Mech. Phys. Solids **60**, 84 (2012).
- [60] J.-H. Seo, Y. Yoo, N.-Y. Park, S.-W. Yoon, H. Lee, S. Han, S.-W. Lee, T.-Y. Seong, S.-C. Lee, K.-B. Lee, et al., Nano Lett. **11**, 34993502 (2011).
- [61] A. T. Jennings, J. Li, and J. R. Greer, Acta Mater. **In Press** (2011).
- [62] J. Diao, K. Gall, and M. Dunn, Nano Lett. **4**, 1863 (2004).
- [63] H. J. Frost and M. F. Ashby, *Deformation mechanism maps: the plasticity and creep of metals and ceramics* (Oxford:Pergamon, 1982).
- [64] R. Becker and W. Döring, Ann. Phys. (Weinheim, Ger.) **24**, 719 (1935).
- [65] S. Glasstone, K. J. Laidler, and H. Eyring, *The theory of rate processes* (McGraw-Hill, 1941).
- [66] P. Hänggi, P. Talkner, and M. Borkovec, Rev. Mod. Phys. **62**, 251 (1990).
- [67] T. Zhu, J. Li, A. Samanta, A. Leach, and K. Gall, Phys. Rev. Lett. **100**, 025502 (2008).
- [68] S. Ryu, K. Kang, and W. Cai, Proc. Natl. Acad. Sci. (USA) **108**, 5174 (2011).
- [69] S. Ryu, K. Kang, and W. Cai, J. Mater. Research (**in press**) (2011).
- [70] A. Ngan, L. Zhuo, and P. Wo, Proc. R. Soc. **462**, 1661 (2006).
- [71] H. Jónsson, G. Mills, and K. W. Jacobsen, *Classical and Quantum Dynamics in Condensed Phase Simulations* (World Scientific, 1998), chap. Nudged elastic band method for finding minimum energy paths of transitions, pp. 385–404.
- [72] W. E, W. Ren, and E. Vanden-Eijnden, Phys. Rev. B **66**, 052301 (2002).
- [73] D. Caillard and J. L. Martin, *Thermally activated mechanisms in crystal plasticity* (Pergamon, 2003).
- [74] J. Marian and J. Knap, International Journal for Multiscale Computational Engineering **5**, 287 (2007).
- [75] E. B. Webb, III, J. A. Zimmerman, and S. C. Seel, Mathematics and Mechanics of Solids **13**, 221 (2008).
- [76] C. R. Weinberger, Acta Mater. **58**, 6535 (2010).
- [77] F. A. Lindemann, Physik. Z **11**, 609 (1910).
- [78] J. Diao, K. Gall, and M. Dunn, Nature Materials **2**, 656 (2003).
- [79] K. Gall, J. Diao, M. Dunn, and M. Haftel, Journal of Engineering Materials and Technology

127, 417 (2005).

- [80] M. Haftel and K. Gall, Physical Review B **74**, 035420 (2006).
- [81] H. Park, Nano Lett **6**, 958 (2006).
- [82] Q. Cheng, H. Wu, Y. Wang, and X. Wang, Applied Physics Letters **95**, 021911 (2009).
- [83] J. S. Bowles and C. M. Wayman, Metall. Mater. Trans. B **3**, 1113 (1972).
- [84] H. K. D. H. Bhadeshia, *Encyclopedia of Materials: Science and Technology* (Elsevier, 2001), pp. 5203–5206.
- [85] J. Christian, *The theory of transformations in metals and alloys : an advanced textbook in physical metallurgy* (Pergamon Press, 2002).
- [86] K. Bhattacharya, *Microstructure of Martensite: Why It Forms and How It Gives Rise to the Shape-Memory Effect* (Oxford University Press, 2003).
- [87] K. Otsuka and X. Ren, Prog. Mater. Sci. **50**, 511 (2005).
- [88] M. Notomi, K. J. van Vliet, and S. Yip, Mater. Res. Soc. Symp. Proc. **980**, 223 (2007).
- [89] W. Liang and M. Zhou, Journal of Engineering Materials and Technology **127**, 423 (2005).
- [90] W. Liang, M. Zhou, and F. Ke, Nano Lett **5**, 2039 (2005).
- [91] Y. G. Zheng, H. W. Zhang, Z. Chen, L. Wang, Z. Q. Zhang, and J. B. Wang, Appl. Phys. Lett. **92**, 041913 (2008).
- [92] Y. Zheng, H. Zhang, Z. Chen, and S. Jiang, Int. J. Multiscale Comput. Eng. **7**, 205 (2009).
- [93] F. F. Csikor, C. Motz, D. Weygand, M. Zaiser, and S. Zapperi, Science **318**, 251 (2007).
- [94] C. R. Weinberger and W. Cai, Nano Letters **10**, 139 (2010).
- [95] C. R. Weinberger and W. Cai, J. Mech. Phys. Solids **58**, 1011 (2010).
- [96] C. R. Weinberger, Int. J. Plasticity **27**, 1391 (2011).
- [97] H. Gao and Y. Huang, Scripta Mater. **48**, 113 (2009).
- [98] J. D. Eshelby, J. Applied Physics **24**, 176 (1953).
- [99] M. S. Duesbery and V. Vitek, Acta Mater. **46**, 1481 (1998).
- [100] W. Cai, V. V. Bulatov, J. Chang, J. Li, and S. Yip, *Dislocations in Solids* (North-Holland Pub., 2004), vol. 12, chap. Dislocation Core Effects on Mobility, p. 1.
- [101] C. R. Weinberger and W. Cai, Proc. Nat. Acad. Sci. USA **105**, 14304 (2008).
- [102] J. R. Greer, C. R. Weinberger, and W. Cai, Mater. Sci. Eng. A **493**, 21 (2008).
- [103] Z. Shan (2011), private communication.
- [104] H. Park, W. Cai, H. Espinosa, and H. Huang, Mrs Bull **34**, 178 (2009).

[105] S. Aubry, S. Ryu, K. Kang, and W. Cai, Scripta Mat. **64**, 1043 (2011).